WAVE-BASED SIMULATION OF A SMALL REVERBERATION ROOM WITH LOCAL AND EXTENDED REACTION MODELING

Jan Wouter Smits[1], Alexandre Wilkinson[2], Arnaud Duval[2]

[1] *The University of Edinburgh, United Kingdom*
[2] *Trèves products services & innovation, France*

This paper is a revised version of the authors' submitted manuscript that was peer-reviewed by at least two anonymous reviewers.

Abstract

A finite-difference room acoustic simulation method is proposed that can model both locally-reacting boundaries and extended-reaction effects via propagation in porous materials. Its suitability for wideband simulations in automotive cabin scenarios is explored by comparing simulations of a small reverberation room with experimental measurements, including configurations with varying absorber geometries and material specifications.

Keywords: *finite differences, reverberation rooms, porous material models, extended reaction*

1. Introduction

Acoustic simulations of automotive cabins often rely on hybrid approaches, in which finite-element methods are used at low frequencies and geometrical-acoustics or statistical-energy methods are used at higher frequencies (see for example [1]). Finite-difference time-domain (FDTD) methods have meanwhile seen improvements in efficiency [2] and boundary-modeling accuracy [3], while recent work has added the capability to model porous-material propagation [4][5]. GPU-accelerated wave-based methods have also been demonstrated [6], but high-frequency simulations in automotive cabin scenarios with extended-reaction porous modeling remain largely unexplored.

The aim of this study is to demonstrate that modern FDTD techniques can enable broadband simulation in an automotive cabin scenario without the need for hybrid methods. The proposed method builds on the extended-reaction formulation of [4], while adding generalized frequency-dependent boundary conditions so that both volumetric porous-material models and locally reacting boundary conditions can be included within the same simulation.

Corresponding author: *jws@possumstudios.com.*

To validate the numerical method, measurements were performed in a small reverberation room with a volume of 6.72 m^3, using three materials in several absorber configurations. Whereas previous studies have demonstrated wave-based finite-element modeling of similar reverberation rooms [7][8] at lower frequencies, the present work investigates wave-based modeling up to 10 kHz within practical computation times.

Section 2 introduces the numerical formulation. Sections 3–5 describe the reverberation room, porous-material models, and experimental procedure. Section 6 compares the simulations and measurements, and examines local- and extended-reaction modeling together with numerical robustness. Conclusions are given in Section 7.

2. Numerical scheme

2.1. Continuous system

The frequency-domain linearized acoustics equations are written as

$$\mathrm{i}\omega\hat{p} = -\hat{K}\nabla\cdot\hat{\boldsymbol{v}} + \hat{Q}_s, \tag{1}$$

$$\mathrm{i}\omega\hat{\boldsymbol{v}} = -\hat{R}\nabla\hat{p}, \tag{2}$$

where $\hat{p}$ and $\hat{\boldsymbol{v}}$ denote pressure and particle velocity, and $\hat{Q}_s$ is a volume velocity source term. The effective bulk modulus $\hat{K}$ and effective inverse density $\hat{R}$ are fluid parameters that can vary with frequency and position. In air they are assumed constant, with $\hat{R} = 1/\rho_0$ and $\hat{K} = \rho_0 c_0^2$ for air density ρ_0 and wavespeed c_0. On the boundary $\partial\Omega$ of the domain Ω, impedance boundary conditions are imposed as

$$\boldsymbol{n}\cdot\hat{\boldsymbol{v}} = \frac{1}{Z_0}\hat{Y}\hat{p}, \quad \boldsymbol{x}\in\partial\Omega, \tag{3}$$

where $\boldsymbol{n}$ is the outward boundary normal vector, $\hat{Y}$ is the normalized (dimensionless) boundary admittance and $Z_0 = \rho_0 c_0$.

To enable time-domain simulation, the frequency-dependent parameters are approximated by passive (positive-real) rational functions

$$\hat{F} \approx F_\infty + \sum_{m=1}^{M_F} \frac{A_F^{(m)}}{\mathrm{i}\omega - \eta_F^{(m)}}, \quad F = R, K, Y, \tag{4}$$

with poles η in the complex left half-plane. This leads to a time-domain system

$$\partial_t p = -K_\infty \nabla \cdot \boldsymbol{v} - \sum_{m=1}^{M_K} A_K^{(m)} \phi_K^{(m)}, \tag{5}$$

$$\partial_t \boldsymbol{v} = -R_\infty \nabla p - \sum_{m=1}^{M_R} A_R^{(m)} \boldsymbol{\phi}_R^{(m)}, \tag{6}$$

$$\boldsymbol{n} \cdot \boldsymbol{v} = \frac{Y_\infty}{Z_0} p + \frac{1}{Z_0} \sum_{m=1}^{M_Y} A_Y^{(m)} \phi_Y^{(m)} \quad \boldsymbol{x} \in \partial\Omega, \tag{7}$$

where the auxiliary state variables $\phi_K, \boldsymbol{\phi}_R, \phi_Y$ are governed by ordinary differential equations

$$\frac{\mathrm{d}\phi_K^{(m)}}{\mathrm{d}t} - \eta_K^{(m)} \phi_K^{(m)} = \nabla \cdot \boldsymbol{v}, \quad m = 1 ... M_K, \tag{8}$$

$$\frac{\mathrm{d}\boldsymbol{\phi}_R^{(m)}}{\mathrm{d}t} - \eta_R^{(m)} \boldsymbol{\phi}_R^{(m)} = \nabla p, \quad m = 1 ... M_R, \tag{9}$$

$$\frac{\mathrm{d}\phi_Y^{(m)}}{\mathrm{d}t} - \eta_Y^{(m)} \phi_Y^{(m)} = p, \quad m = 1 ... M_Y. \tag{10}$$

Observe that ϕ_K, ϕ_Y are scalar quantities, whereas $\boldsymbol{\phi_R}$ is a vector.

2.2. Discretization

A staggered finite-difference discretization is employed on an FCC grid, which improves numerical isotropy and reduces dispersion error compared to Cartesian grids [2], [9]. Scalar quantities (pressure and scalar auxiliary states) are defined at grid nodes $\boldsymbol{x_i} = \boldsymbol{i}X$, with index set

$$\mathcal{I} = \{\boldsymbol{i} \in \mathbb{Z}^3 | (i_1 + i_2 + i_3) \bmod 2 = 0, \boldsymbol{i}X \in \Omega\}. \tag{11}$$

Each node $\boldsymbol{i}$ has 12 nearest neighbors at $\boldsymbol{i} + \boldsymbol{j}$, where $\boldsymbol{j} \in \mathbb{Z}^3, \|\boldsymbol{j}\|_2^2 = 2$. Vector quantities (velocity and vector auxiliary states) are defined at interlaced locations $(\boldsymbol{i} + \boldsymbol{j}/2)X$. In the following, vector variables are indexed by 3-D stencil index $\boldsymbol{j}$, such that $v_{\boldsymbol{i},\boldsymbol{j}}$ indicates the scalar component associated with the neighbor index offset $\boldsymbol{j}$.

Spatial differences are now defined for generic scalar and vector variables $u_{\boldsymbol{i}}, \boldsymbol{w_i}$ respectively by

$$D_{\boldsymbol{j}}^{\pm} u_{\boldsymbol{i}} = \frac{\pm 1}{\sqrt{2}X} (u_{\boldsymbol{i} \pm \boldsymbol{j}} - u_{\boldsymbol{i}}), \tag{12}$$

$$D_{\boldsymbol{j}} \boldsymbol{w_i} = \frac{1}{\sqrt{2}X} (w_{\boldsymbol{i},\boldsymbol{j}} - w_{\boldsymbol{i},-\boldsymbol{j}}), \tag{13}$$

leading to discrete gradient and divergence operators

$$(D_\nabla u_{\boldsymbol{i}})_{\boldsymbol{j}} = D_{\boldsymbol{j}}^+ u_{\boldsymbol{i}}, \quad D_\nabla \cdot \boldsymbol{w_i} = \frac{1}{2} \sum_{\boldsymbol{j} \in \mathcal{R}'} D_{\boldsymbol{j}} \boldsymbol{w_i}, \tag{14}$$

where $\mathcal{R}'$ contains one vector from each anti-parallel pair $\{\boldsymbol{j}, -\boldsymbol{j}\}$.

Time is discretized with step T, with scalar variables at integer time $t^n = nT, n \in \mathbb{N}$ and vector variables at interlaced times $t^{n+\frac{1}{2}} = (n+\frac{1}{2})T$. Temporal operators are defined as

$$D_t^{\pm} = \frac{\pm 1}{T} (u^{n \pm 1} - u^n), \quad M_t^{\pm} u^n = \frac{1}{2} (u^{n \pm 1} + u^n). \tag{15}$$

2.3. Discrete system

Applying the above operators to (5)-(10) yields the difference equations

$$D_t^+ p_{\boldsymbol{i}}^n = -K_{\infty,\boldsymbol{i}} D_\nabla \cdot \boldsymbol{v}_{\boldsymbol{i}}^{n+\frac{1}{2}} - \sum_{m=1}^{M_K} A_{K,\boldsymbol{i}}^{(m)} M_t^+ \phi_{K,\boldsymbol{i}}^{(m),n}, \tag{16}$$

$$D_t^- v_{\boldsymbol{i},\boldsymbol{j}}^{n+\frac{1}{2}} = -R_{\infty,\boldsymbol{i},\boldsymbol{j}} D_{\boldsymbol{j}}^+ p_{\boldsymbol{i}}^n - \sum_{m=1}^{M_R} A_{R,\boldsymbol{i},\boldsymbol{j}}^{(m)} M_t^- \phi_{R,\boldsymbol{i},\boldsymbol{j}}^{(m),n+\frac{1}{2}}, \tag{17}$$

with boundary condition

$$v_{\boldsymbol{i},\boldsymbol{j}}^{n+\frac{1}{2}} = \frac{\boldsymbol{n} \cdot \boldsymbol{j}}{Z_0 \sqrt{2}} \left(Y_\infty p_{\boldsymbol{i}}^n + \sum_{m=1}^{M_y} A_{Y,\boldsymbol{i}}^{(m)} M_t^+ \phi_{Y,\boldsymbol{i}}^{(m),n} \right). \tag{18}$$

for nodes where $(\boldsymbol{i} + \boldsymbol{j})X \notin \Omega$, following the surface-area compensation approach described in [3].

The auxiliary state equations are discretized using the trapezium rule as

$$D_t^+ \phi_{K,\boldsymbol{i}}^{(m),n} - \eta_{K,\boldsymbol{i}}^{(m)} M_t^+ \phi_{K,\boldsymbol{i}}^{(m),n} = D_\nabla \cdot \boldsymbol{v}_{\boldsymbol{i}}^{n+\frac{1}{2}}, \tag{19}$$

$$D_t^+ \boldsymbol{\phi}_{R,\boldsymbol{i},\boldsymbol{j}}^{(m),n-\frac{1}{2}} - \eta_{R,\boldsymbol{i},\boldsymbol{j}}^{(m)} M_t^+ \boldsymbol{\phi}_{R,\boldsymbol{i},\boldsymbol{j}}^{(m),n-\frac{1}{2}} = D_{\boldsymbol{j}}^+ p_{\boldsymbol{i}}^n, \tag{20}$$

$$D_t^+ \phi_{Y,\boldsymbol{i}}^{(m),n} - \eta_{Y,\boldsymbol{i}}^{(m)} M_t^+ \phi_{Y,\boldsymbol{i}}^{(m)} = M_t^+ p_{\boldsymbol{i}}^n. \tag{21}$$

After expansion of the operators, the above discrete system can be rearranged to form a set of update equations that are solved in an explicit time-stepping loop. In homogeneous regions, the expressions reduce to scalar two-step updates [4], [5], which greatly benefits computational efficiency.

3. Reverberation room

The room used in this study has an irregular hexahedron shape with six non-parallel walls. Four diffusing profiles are attached to the walls and a cone is attached to the ceiling, as seen in Fig. 1a. Four speakers are integrated in corners of the room and an omnidirectional microphone attached to a boom can be rotated to six different measurement positions. The internal volume of the room is 6.72 m^3.

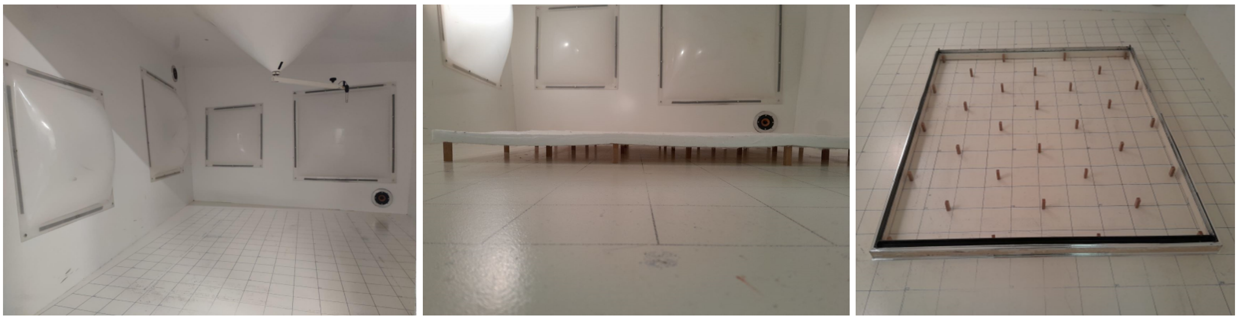

(a) (b) (c)

Figure 1: Photographs of the reverberation room: (a) internal view showing the wall diffusers, ceiling cone and microphone arm; (b) configuration G4NF (with airgap and no frame); (c) frame and spacers used in configuration G4.

4. Porous absorbers

4.1. Material properties and configurations

Three porous materials were used, two of which are characterized in table 1. Sheets of size 1.2m by 1.0m were cut from these materials and placed horizontally in the center of the room according to the five different configurations shown in Table 2. In configurations G1 and G2, a single sheet was placed directly on the floor and in configuration G3 a sandwich of two materials was used. In configurations G4 and G4NF, the material sample was placed on small spacers in order to create an airgap. In all configurations except G4NF (pictured in Fig. 1b), a thin metal frame was placed around the sample in order to acoustically shield the edges.

4.2. Equivalent-fluid modeling

The porous material is modeled using the Johnson–Champoux–Allard (JCA) equivalent-fluid model [10], with parameters given in Table 1: flow resistivity σ, porosity ϕ, tortuosity α_∞, and viscous and thermal characteristic lengths Λ and Λ'. Vector fitting [11] was used to fit $\hat{R}$ and $\hat{K}$ with rational functions. Two poles were found sufficient for accurate fits.

4.3. Local-reaction approximation

The local-reaction approximation requires the admittance $\hat{Y}$ to be independent of the field-incidence angle. To obtain this function, we first derive an incidence-dependent admittance $\hat{Y}_E(\theta)$ by applying the transfer-matrix (TMM) method [12] with the thickness and EFM parameters of each layer as input. Subsequently, $\hat{Y}_E$ is averaged over the solid angle, as described in [13], assuming diffuse incidence:

$$\hat{Y} = \frac{\int_0^{\theta_f} \hat{Y}_E(\theta)\sin(\theta)\mathrm{d}\theta}{1-\cos(\theta_f)}. \qquad (22)$$

In the final approximation step, $\hat{Y}$ is again fitted with a rational function, using up to ten poles.

Fig. 2 compares the resulting angle-independent local-reaction (LR) admittance derived from (22) to the range of TMM-computed extended-reaction (ER) admittances for configuration G1. The figure also shows the diffuse absorption values computed for both cases through the well-known Paris formula.

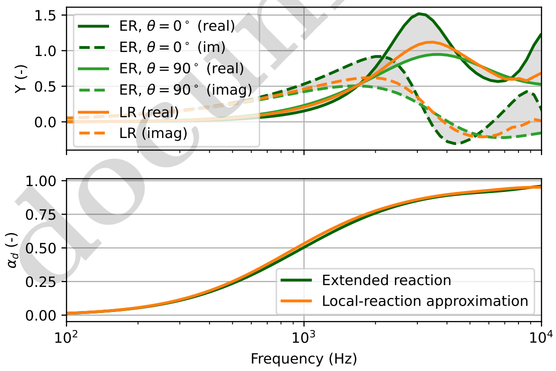

Figure 2: Theoretical extended-reaction (ER) admittance of infinite absorber configuration G1, compared to local-reaction (LR) approximation. The bottom panel shows the theoretical diffuse absorption values for both.

5. Measurements

To generate the experimental absorption values, measurements were taken according to Renault Group standard D49 1997 [14], through an interrupted pink noise method exciting the four loudspeakers integrated in the room. Reverberation times were then computed in third-octave bands from 400 Hz to 10 kHz and averaged across the six microphone positions. The averaged decay times were subsequently converted to absorption coefficients according to the Sabine relation

$$\alpha_s = \frac{55.3V}{c_0 S}\left(\frac{1}{T_{\mathrm{trim}}} - \frac{1}{T_{\mathrm{bare}}}\right) \qquad (23)$$

where V is the volume of the room, S is the surface area of the material sample, T_{bare} is the reverberation time without the material sample present, and T_{trim} is the reverberation time with the material sample.

An additional set of measurements was performed with a Simcenter Qind2 monopole source in order to obtain accurate frequency response measurements for

Table 1: Material parameters measured in impedance tube.

Porous material	σ (Ns/m^4)	ϕ	α_∞	Λ (μm)	Λ' (μm)	ρ (kg/m^3)	E (kPa)
CF_20	21399	0.955	1.0	67.1	79.5	48.4	9.48
F4_5	172982	0.934	1.0	16.6	83.8	88.6	5.36

Table 2: Configuration of absorbers. In G3, material #1 is placed on top and material #2 is on bottom.

Configuration	material #1	thickness #1 (mm)	material #2	thickness #2 (mm)	airgap (mm)	frame height (mm)
G1	CF_20	21.4				20
G2	F4_5	5.9				10
G3	F4_5	5.9	CF_20	21.4		30
G4	F4_20	20.5			40	60
G4NF	F4_20	20.5			40	

comparison with simulation. For these measurements, the monopole source was placed in front of the integrated loudspeaker positions, and frequency response functions were obtained at the microphone positions between 100 Hz and 10 kHz using a white noise excitation method. Reverberation times were computed from these measurements as a cross-validation and verified to be close to those measured with the integrated speakers and interrupted noise method.

6. Simulations

Simulations were performed using a GPU-based software implementation of the finite-difference method discussed in Section 2. The program was developed as a C++ and CUDA-based library with a Python interface, and incorporates a voxelization module for arbitrary mesh-geometry inputs. All simulations were performed with a grid step-size of $X = 2$mm and time step $T = 28.8\mu s$, chosen to satisfy the CFL stability condition and ensure numerical dispersion error below 0.8% in the worst-case propagation direction up to 20 kHz, as evaluated through von Neumann analysis (see [2]). Sub-voxel-scale random perturbations are introduced to the porous-material geometry to reduce coherent discretization bias (analogous to dithering), improving the modeling accuracy of thin structures. The simulation results shown in the next section were computed on an RTX5090 GPU device and take around 70 minutes to compute a 3 seconds-long impulse response.

6.1. Absorption-value simulation results

To compute simulated absorption values, four simultaneously-driven point sources were positioned close to the locations of the integrated speakers at the same locations as the experimental monopole sources. The sources were driven with a wideband impulse and absorption values were then derived in the same manner as for the measurements, by averaging the decay time computed at each microphone position and converting to absorption with Eq. (23).

Fig. 3 shows a comparison of the Sabine absorption computed from the measurements and the simulations for absorber configurations G1-G3. Differences between the measurements and simulations are generally less than 0.1 absorption units, with some larger excursions visible at 500Hz for configurations G1 and G3 and around 2 kHz for G1. Since numerical discretization errors at these frequencies are small, the deviations are likely due to measurement or modeling uncertainties. Another observation is that the local-reaction simulations are generally close to the extended-reaction results, which is expected given the small height of the absorbers. Some larger differences between local and extended reaction results are seen for the sandwich configuration G3, where the extended-reaction results are close to the measurements while the local-reaction approximation deviates between 620 Hz and 1 kHz.

Fig. 3 also compares the measured and simulated absorption values to absorption computed with the finite-size TMM (FTMM) method described in [15]. The FTMM method improves over the TMM method by taking into account the finite size of the sample, which is important here due to the small sample dimensions. Compared to FDTD simulation, the FTMM calculation still makes simplified assumptions about the absorber geometry and assumes a perfectly random incidence.

Results for the configurations G4 and G4NF, which include a 40mm airgap behind a porous material layer are shown in Fig. 4. This type of absorber configuration is expected to show a more pronounced extended-reaction effect, and the extended-reaction simulations are indeed closer to the measurements, especially when the frame is removed. In the case without frame, the FTMM method deviates very significantly, confirming that its assumptions about edge effects break down and a volumetric discretization as provided by the FDTD method is necessary.

6.2. Frequency-response simulation

For applications like auralization, it is not enough to predict decay times but frequency and impulse responses must also be accurately reproduced. As part of this study, frequency response functions were measured using a compact broadband monopole source, as described in section 5. This measurement is compared with the simulated frequency response in Fig. 5, showing a good match over the range between 80 Hz and 1 kHz. At frequencies above 1 kHz details of the curves become more separated because of high modal density and sensitivity to small geometrical differences between the model and reality.

6.3. Sensitivity to grid resolution

To investigate the numerical robustness of the scheme, Fig. 6 shows the simulated absorption for different grid resolutions. Between the resolutions of 2 mm and 3 mm the results appear converged except for a small deviation around 3 kHz which is related to geometrical roundoff in the frame dimensions. At $X = 8$ mm significant errors appear, especially for the extended-reaction computation which has insufficient resolution to correctly model the 21.4 mm thick porous layer. As a general rule we find that for extended-reaction modeling of a panel with thickness h the resolution X should preferably be set to $h/8$ or less. The reduced propagation speed in porous media must also be taken into account. With X=2 mm, the grid resolution provides at least 7 and 5 points per wavelength (PPW) at 10 and 20 kHz, respectively, for the slowest of the three materials.

7. Conclusions

A finite-difference method was presented that incorporates both extended-reaction modeling of porous absorbers and general frequency-dependent locally-reacting boundary conditions. Simulations of a small reverberation room including diffusing structures are demonstrated with a grid resolution of 2 mm, corresponding to numerical dispersion below 0.8% in air up to 20 kHz. The simulated frequency response shows good correlation with measurements up to 1 kHz, indicating accurate modeling of the room's modal behavior. Agreement with the measured absorption values up to 10 kHz further demonstrates accurate reproduction of the room's acoustic behavior, including wave propagation in the porous material.

References

[1] A. Peiffer, *Vibroacoustic Simulation: An Introduction to Statistical Energy Analysis and Hybrid Methods*. Wiley, 2022.

[2] B. Hamilton and S. Bilbao, "On finite difference schemes for the 3-D wave equation using non-Cartesian grids," in *Proc. Sound and Music Computing Conf. (SMC)*, Stockholm, Sweden, 2013, pp. 592–599.

[3] J. W. Smits, "Compensation of staircase-induced boundary absorption errors in FDTD simulation," in *Proc. INTER-NOISE*, Nantes, France, 2024.

[4] J. W. Smits, "Efficient finite-difference room acoustics simulation incorporating extended-reacting elements," in *Proc. Digital Audio Effects (DAFx)*, Copenhagen, Denmark, 2023.

[5] J. W. Smits, "Wideband acoustic simulation of anechoic chambers using a finite-difference method with porous media modeling," *Proc. Meet. Acoust.*, vol. 56, no. 1, 2025.

[6] C. Webb and S. Bilbao, "Computing room acoustics with CUDA - 3D FDTD schemes with boundary losses and viscosity," in *Proc. IEEE ICASSP*, Prague, Czech Republic, 2011, pp. 317–320.

[7] A. Duval, J.-F. Rondeau, L. Dejaeger, F. Sgard, and N. Atalla, "Diffuse field absorption coefficient simulation of porous materials in small reverberant rooms: Finite size and diffusivity issues," Lyon, France: 10e Congrès Français d'acoustique, 2010.

[8] C. Bertolini, "Numerical simulation of the measurement of the diffuse field absorption coefficient in small reverberation rooms," *SAE Int. J. Passeng. Cars, Mech. Syst.*, vol. 4, pp. 1168–1194, 2011.

[9] B. Hamilton, "Finite volume perspectives on finite difference schemes and boundary formulations for wave simulation," in *Proc. Digital Audio Effects (DAFx)*, Erlangen, Germany, 2014, pp. 295–302.

[10] Y. Champoux and J.-F. Allard, "Dynamic tortuosity and bulk modulus in air-saturated porous media," *J. Appl. Phys.*, vol. 70, no. 4, pp. 1975–1979, 1991.

[11] B. Gustavsen and A. Semlyen, "Rational approximation of frequency-domain responses by vector fitting," *IEEE Trans. on Power Delivery*, vol. 14, pp. 1052–1061, 1999.

[12] J. Allard and N. Atalla, *Propagation of sound in porous media: modelling sound absorbing materials*, 2nd ed. John Wiley & Sons, 2009.

[13] M. Aretz and M. Vorlaender, "Efficient modelling of absorbing boundaries in room acoustic fe simulations," *Acta Acustica united with Acustica*, vol. 96, pp. 1042–1050, 2010.

[14] D49 1997, "Fibrous and cellular materials sound absorption in diffuse field," Renault Group, Tech. Rep., 1997.

[15] Y. Yu and C. Hopkins, "Reduced order integration for the radiation efficiency of a rectangular plate," *JASA Express Letters*, vol. 1, p. 062 801, 2021.

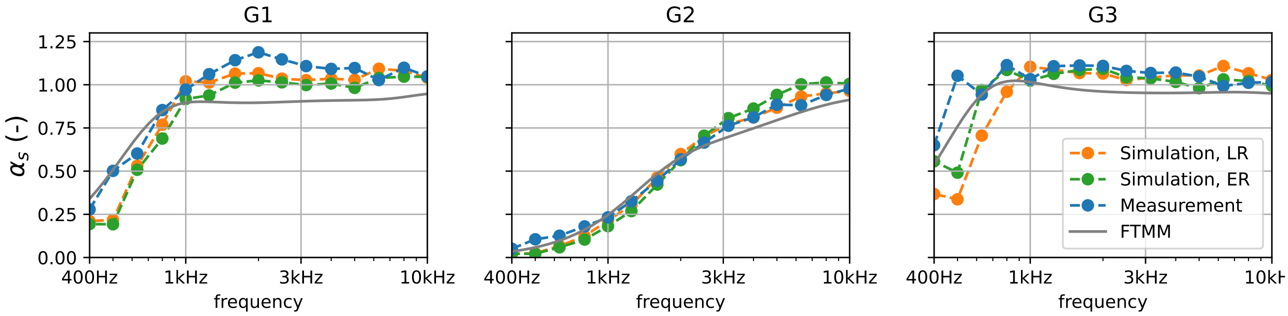

Figure 3: Simulated Sabine absorption with local (LR) and extended reaction (ER) for three different absorbers, compared to measurement and to theoretical FTMM approximation.

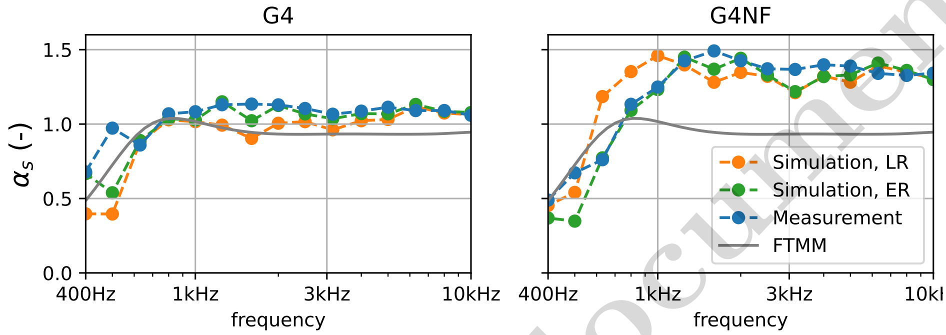

Figure 4: Measured and simulated Sabine absorptions for the configuration with (G4) and without (G4NF) metal frame around the absorber.

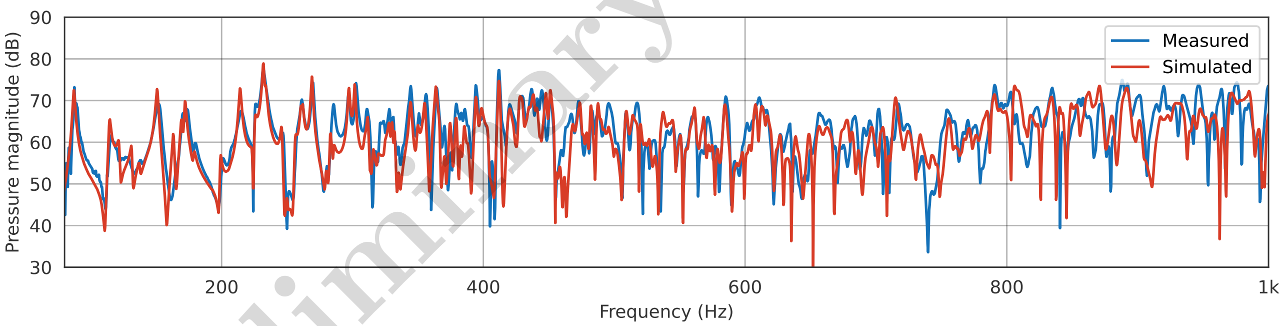

Figure 5: Frequency response comparison to measurements with absorber configuration G1.

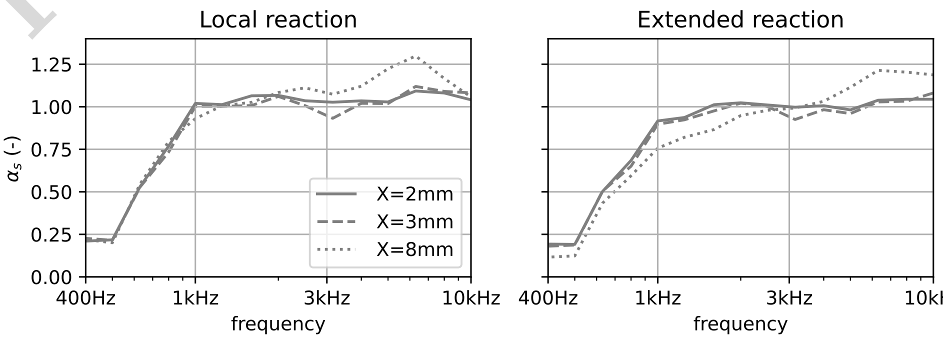

Figure 6: Variation of simulated absorption values as a function of grid resolution for absorber G1.